Astron. Astrophys. 356, 579–584 (2000)

ASTRONOMY AND ASTROPHYSICS

# On the secondary star of the galactic supersoft X-ray source RX J0925.7−4758 and Doppler tomography of the emission lines⋆

**K. Matsumoto**[1] **and R.E. Mennickent**[2]

[1] Department of Astronomy, Faculty of Science, Kyoto University, Kyoto 606-8502, Japan (katsura@kusastro.kyoto-u.ac.jp)
[2] Departamento de Física, Universidad de Concepción, Casilla 160-C, Concepción, Chile (rmennick@stars.cfm.udec.cl)

Received 17 November 1999 / Accepted 11 January 2000

**Abstract.** We carried out optical spectroscopic observations of the galactic supersoft X-ray source RX J0925.7−4758. The relatively long orbital period among supersoft X-ray sources was confirmed. The nature of the secondary star is discussed using its invisibility in the optical spectrum. Under the hypothesis of a non-eclipsing white dwarf, we derived an A–G giant secondary with an inclination angle of $55^\circ \pm 10^\circ$. Doppler maps of the He II $\lambda 4686$ and H$\alpha$ emission lines were constructed, which generally resemble those of RX J0019.8+2156, suggesting a common line emitting region in supersoft X-ray sources. The concentration of the main emission region to low-velocities indicates that the mass function gives only a lower limit to the mass of the secondary star.

**Key words:** accretion, accretion disks – stars: binaries: close – stars: individual: RX J0925.7-4758 – X-rays: stars

## 1. Introduction

Supersoft X-ray sources (hereafter called as SSXSs) are characterized by their luminous X-rays near the Eddington limit with extremely low black-body temperature less than $100$ eV (Kahabka & van den Heuvel 1997 for a review). They were discovered and manifested by the *Einstein* Observatory and ROSAT. The systems are considered as binaries containing a mass accreting white dwarf and a mass donor secondary star (van den Heuvel et al. 1992; Rappaport et al. 1994). The matter from the secondary star forms an accretion disk around the white dwarf with a moderate mass accretion rate of order of $10^{-7}\ M_\odot\ \mathrm{yr}^{-1}$ for steady nuclear burning on the surface. The condition brings a gradual increase of mass of the relatively high mass white dwarf, and it has been suggested that SSXSs will become type Ia supernovae when the mass of the white dwarf exceeds the Chandrasekhar limit (Li & van den Heuvel 1997; Hachisu et al. 1999).

SSXSs are mostly detected in the Magellanic clouds and M 31 because strong interstellar absorption of the low temperature X-rays prevents us from detecting them in our Galaxy even in short distances. RX J0925.7−4758 (hereafter called as RX J0925) is one of the galactic SSXSs discovered in the ROSAT all sky survey (Motch et al. 1994). This object located toward the Vela molecular cloud has $m_\mathrm{V} \sim 17$ and is highly reddened. Its optical spectrum resembles those of other SSXSs, including the transient bipolar jets (Motch 1998), except for its highly reddened continuum. Such high velocity features were also observed in other SSXSs: permanent jet features in RX J0513.9−6951 (Crampton et al. 1996) and transient jets in RX J0019.8+2156 (Tomov et al. 1998; Becker et al. 1998). The photometric observations of RX J0925 suggested that the orbital period is 3.79 ± 0.24 d and the radial velocity study also indicated a similar value (Motch et al. 1994; Motch 1996). Ebisawa et al. (1996) concluded, from their ASCA observation, that the object has a massive white dwarf near the Chandrasekhar limit with a distance of more than 10 kpc. A near-the-limit white dwarf was also expected theoretically to explain the observed data by ASCA (Hoshi 1998). Hartmann et al. (1999) argued that the effective temperature should be $\sim 10^6$ K and a second spectral component is required to explain the X-ray spectrum from the BeppoSAX observation.

We carried out optical spectroscopy of this object in order to get the system parameters which have not been well known because of its relatively long orbital period. The observations are described in Sect. 2, and the results and discussions, including Doppler imaging of the emission lines, are presented in Sect. 3.

## 2. Observations

The observations were made during nine nights using the ESO 3.5-m NTT at La Silla observatory. The observing time was divided into two runs: the first run between April 16 and 20 and the second run between May 29 and 31, 1998. The EMMI at red medium dispersion mode (REMD), grating #13, and the red arm CCD camera #36 were selected. This REMD setup and the slit width of one arcsecond yielded a spectral resolution of about $5.5$ Å. The spectral range covered was 4188–9623 Å. Dr. T. Shahbaz kindly provided us two additional spectra obtained by the grating #7 on June 1 1998 with a spectral resolution of about $1.3$ Å and a wavelength coverage of 5784–7118 Å. In total we obtained 32 object frames. A He-Ar comparison spectrum per every scientific exposure was taken for wavelength calibrations.

*Send offprint requests to*: K. Matsumoto

⋆ Based on observations obtained at ESO La Silla Observatory (ESO Proposal 61.D-0397).

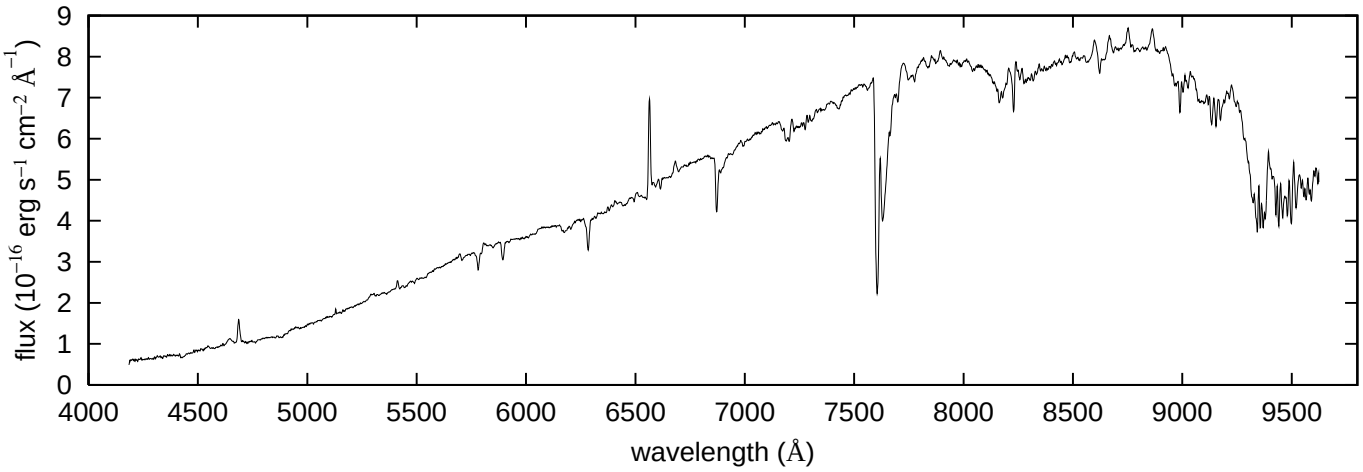


**Fig. 1.** Averaged optical spectrum of RX J0925.

The exposure time for the object was 900–3600 s depending on the sky condition. The other calibration frames of bias and flat images were taken during day time.

The data reduction was performed in a standard manner using IRAF[1]. Tasks in the *images* and *noao.onedspec* packages were mainly used. All of the two dimensional raw frames were de-biased and flat-fielded using the normalized flat images, and then one dimensional spectra were extracted. Flux calibrations were performed with LTT 3218 as a standard star, but the sky conditions which slightly varied in the nights may affect the individual flux levels. The spectra were finally normalized to the continuum prior to the radial velocity and emission strength analyses. Velocities referred to the Local Standard of Rest were used for the analyses presented in this paper.

## 3. Results and discussions

### *3.1. Optical spectral features*

Fig. 1 shows an averaged spectrum of the object. The spectrum is characterized by emission lines of H$\alpha$, He I, He II, and N III–C III complex at $\sim$ 4640 Å, which are commonly seen in the optical spectra of SSXSs, on the highly reddened continuum. The slope of the flux distribution is about $2 \times 10^{-19}$ erg s$^{-1}$ cm$^{-2}$ Å$^{-1}$/Å at the wavelength range of 4500–8000 Å. We can also recognize emission features of He II $\lambda$5413, He I $\lambda$6678, and the Paschen series. The absence or extreme weakness of H$\beta$ is worthy of remark. The H$\alpha$ emission line was accompanied with a P-Cygni absorption feature typically extended to $\sim$2000 km s$^{-1}$ at the blue wing. No bipolar high velocity emission component was detected in all our object frames. This implies that the possible jet feature is really a transient one, as suggested by Motch (1998). Mean equivalent widths and $FWHM$ of the main emission lines are summarized in Table 1. No significant change of these quantities was detected throughout the observation.

**Table 1.** Mean equivalent widths and $FWHM$ of the main emission lines.

| Line | $EW$ (Å) | $FWHM$ (km s$^{-1}$) |
|---|---|---|
| He II $\lambda$4686 | 6–7 | 570–640 |
| O VI $\lambda$5291 | $\leq$0.5 | $\sim$340 |
| He II $\lambda$5413 | $\sim$1 | $\sim$330 |
| H$\alpha$ | 4–5 | 370–410 |
| He I $\lambda$6678 | $\sim$0.7 | $\sim$450 |

A number of absorption lines apart from the atmospheric lines can plausibly be identified as diffuse intersteller bands. The $\lambda$5779 absorption line indicates $E$(B−V) = 1.94 $\pm$ 0.17, which is consistent with the previous estimation (Motch 1994).

No firm detection of stellar absorption lines of the secondary star was made in the spectra. We will utilize this fact to give a constraint for the nature of the secondary star in Sect. 3.3.

### *3.2. Radial velocities*

In order to estimate the orbital period and other parameters of the binary system, we measured the radial velocities of the He II $\lambda$4686 and H$\alpha$ lines. The radial velocities $v_{\rm RV}$ were estimated using a single gaussian profile fit to every emission line. Resulting radial velocities are given in Table 2 with the observing log (the spectroscopic phase is defined in the next subsection). Assuming a circular orbit, we then fitted them by sinusoidal curves in order to find the orbital period $P_{\rm orb}$, the semi-amplitude $K_1$, and the systemic velocity $\gamma$, using

$$v_{\rm RV} = K_1 \sin(2\pi\Phi) + \gamma, \quad (1)$$

where $\Phi$ represents a phase. Weights corresponding to the spectrum's signal to noise ratio were applied. Fig. 2 shows the periodograms of the He II $\lambda$4686 and H$\alpha$ in the form of $\chi^2$ versus trial period. Their respective minima correspond to 3.72 and 3.71 d, being consistent within their errors. The results of the

[1] IRAF is distributed by the National Optical Astronomy Observatories, which are operated by the Association of Universities for Research in Astronomy, Inc., under cooperative agreement with the National Science Foundation.

**Table 2.** Observing log of the object frames. Date, $HJD$ ($-2450900$) of the mid-exposure time ($HJD_{\rm mid}$), the exposure time in seconds ($exp$), the radial velocities of the He II $\lambda4686$ ($v_{\rm He\,II}$) and H$\alpha$ ($v_{\rm H\alpha}$) emission liens in km s$^{-1}$, and the corresponding spectroscopic phase ($\Phi_{\rm spec}$). There are a few blanks for the velocities, due to fatal noise events in the spectroscopic lines.

| Date (1998) | | $HJD_{\rm mid}$ | $exp$ | $v_{\rm He\,II}$ | $v_{\rm H\alpha}$ | $\Phi_{\rm spec}$ |
|---|---|---|---|---|---|---|
| April | 16 | 20.512 | 900 | 124 | 100 | 0.84 |
| | 16 | 20.525 | 900 | 121 | 84 | 0.84 |
| | 16 | 20.536 | 900 | 140 | 91 | 0.85 |
| | 16 | 20.548 | 900 | 119 | 100 | 0.85 |
| | 16 | 20.594 | 3600 | 150 | 103 | 0.86 |
| | 16 | 20.651 | 3600 | 134 | 98 | 0.88 |
| | 16 | 20.693 | 3600 | 169 | 104 | 0.89 |
| | 17 | 21.492 | 1800 | −17 | −14 | 0.10 |
| | 17 | 21.519 | 1800 | −27 | −11 | 0.11 |
| | 17 | 21.549 | 1800 | −34 | −12 | 0.12 |
| | 17 | 21.572 | 1800 | −93 | −26 | 0.12 |
| | 17 | 21.602 | 1800 | −48 | −42 | 0.13 |
| | 17 | 21.625 | 1800 | −58 | −37 | 0.14 |
| | 17 | 21.649 | 1800 | −132 | −31 | 0.15 |
| | 18 | 22.491 | 1800 | 52 | 13 | 0.37 |
| | 18 | 22.696 | 1800 | 57 | 21 | 0.43 |
| | 19 | 23.499 | 3600 | 146 | 84 | 0.64 |
| | 19 | 23.716 | 1800 | 154 | 82 | 0.70 |
| | 20 | 24.502 | 1800 | 145 | 82 | 0.91 |
| | 20 | 24.676 | 3600 | 106 | 71 | 0.96 |
| May | 29 | 63.488 | 1800 | 42 | −1 | 0.39 |
| | 29 | 63.518 | 1800 | −99 | 8 | 0.40 |
| | 29 | 63.540 | 1800 | −87 | −9 | 0.41 |
| | 30 | 64.486 | 1800 | 170 | 93 | 0.66 |
| | 30 | 64.511 | 1800 | – | 86 | 0.67 |
| | 30 | 64.549 | 1800 | 107 | – | 0.68 |
| | 30 | 64.572 | 1800 | – | 80 | 0.68 |
| | 31 | 65.479 | 1800 | – | 51 | 0.93 |
| | 31 | 65.507 | 1800 | 7 | 24 | 0.94 |
| | 31 | 65.617 | 1800 | – | 25 | 0.96 |
| June | 1 | 66.492 | 3600 | – | −26 | 0.20 |
| | 1 | 66.537 | 3600 | – | −32 | 0.21 |

fitting are summarized in Table 3. A significant difference in $K_1$ between two lines is remarkable. Such a semi-amplitude of He II $\lambda4686$ larger than that of H$\alpha$ was also suggested by Motch (1994).

### *3.3. On the binary system*

We next attempt to set constraints on the system elements. In a simple view of an accretion disk, a higher excitation line is likely to be produced in a hotter region, i.e. the inner part. The different $K_1$ values pointed out in Table 3 may suggest that a more highly ionized line has a larger semi-amplitude, more likely associated with the white dwarf. The O VI $\lambda5291$ line may be a better tracer of the orbital motion, but unfortunately its weakness did not permit us to get meaningful radial velocities. We first assumed that the variation of the He II $\lambda4686$ follows

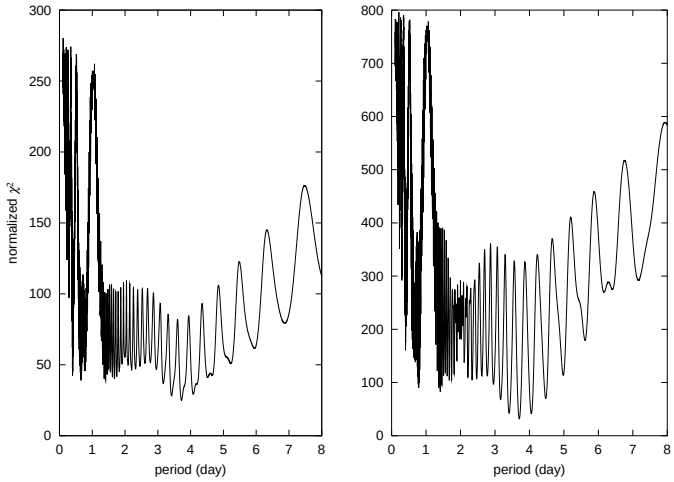


**Fig. 2.** Periodogram for the radial velocity variations of the He II $\lambda4686$ (left) and H$\alpha$ (right) emission lines, which were produced by the $\chi^2$ test.

**Table 3.** Summary of the sinusoidal fitting of the radial velocity variations. The modulation periods, semi-amplitudes, and systemic velocities are given.

| Line | $P_{\rm orb}$ (d) | $K_1$ (km s$^{-1}$) | $\gamma$ (km s$^{-1}$) |
|---|---|---|---|
| He II $\lambda4686$ | $3.72 \pm 0.11$ | $122 \pm 19$ | $33 \pm 10$ |
| H$\alpha$ | $3.71 \pm 0.09$ | $70 \pm 5$ | $32 \pm 3$ |

the orbital motion of the hot component. The radial velocity curves folded on the orbital period for He II $\lambda4686$ and H$\alpha$ are presented in Fig. 3. The moment when $v_{\rm RV} - \gamma$ changes from positive to negative was estimated as $HJD = 2450921.11(2)$. We define this moment as the spectroscopic phase $\Phi_{\rm spec} = 0$.

The mass function of the binary system is $f(M) = 0.77(28)\ M_\odot$ when $P_{\rm orb}$ and $K_1$ of He II $\lambda4686$ are used. As for the mass of the white dwarf $M_1$, a mass near the Chandrasekhar limit was suggested based on the studies in X-rays (Ebisawa et al. 1996; Hoshi 1998). We therefore assume a massive white dwarf of $M_1 = 1.44\ M_\odot$. From this a relation between the inclination angle and mass of the secondary star $M_2$ was derived, and a relation between $M_2$ and radius of the secondary star ($R_2$) was also fixed under the assumption that the secondary star fills its Roche lobe (Fig. 4).

These relations indicate that $M_2$ should be larger than $\sim 1.5\ M_\odot$ and the secondary star is evolved. We can estimate luminosities, surface effective temperatures, and $\log\ g$ for the $M_2$–$R_2$ set using stellar evolution calculations. Color and luminosity classes yield a template spectrum, from which we infer the most dominant absorption features of the secondary star. A lower limit on the luminosity ratio between the contribution from the secondary star and the primary is estimated using the invisibility of the secondary's spectral features (e.g., Katahira et al. 1996).

Template spectra for various spectral types were obtained from the machine-readable data of Jacoby et al. (1984) and Silva & Cornell (1992). We initially intended to use the Ca II

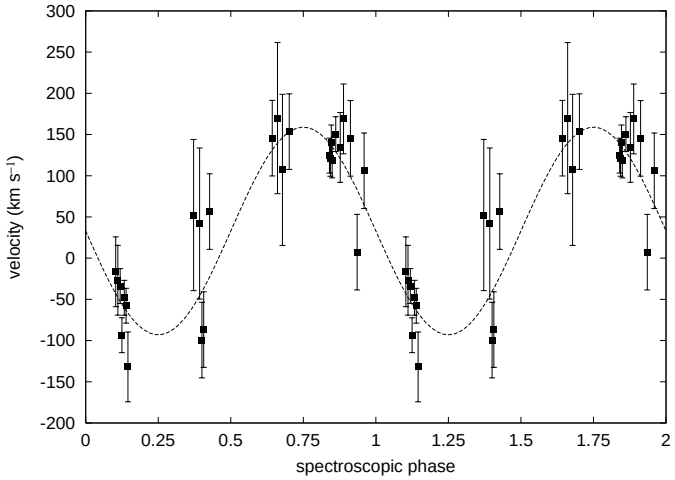


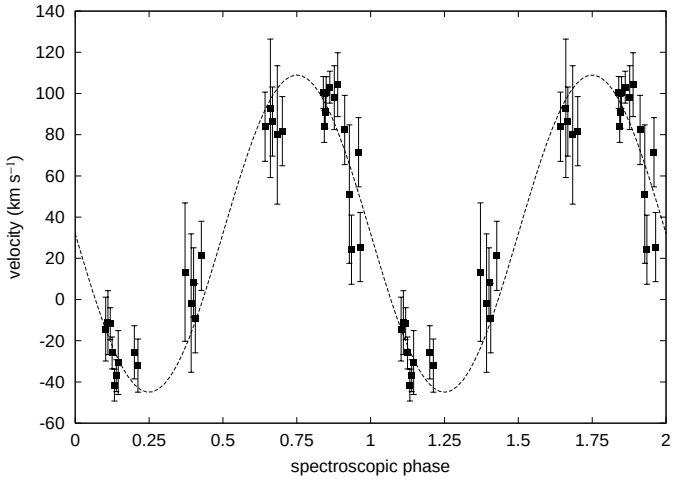


**Fig. 3.** Radial velocity curves of the He II $\lambda 4686$ (top) and H$\alpha$ (bottom) folded on the orbital period. The spectroscopic phase is repeated twice for clarity.

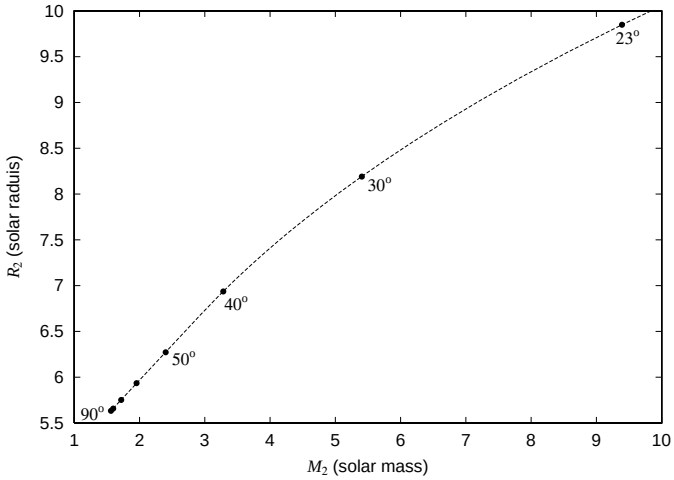


**Fig. 4.** A relation between mass and radius of the secondary star based on the mass function for a fixed 1.44 $M_\odot$ white dwarf (the dashed line). The corresponding inclination angles of 23, 30, 40, 50, 60, 70, 80, and 90° are also plotted. Note 60–80° are not labeled.

**Table 4.** A summary of the constraints for the binary parameters. The values of $M_2, R_2$, and $T_2$ for representative inclination angles, based on the mass function, are given. The luminosity ratio $L_2/L_{2_{\rm mf}}$ and the expected lower limit of the distance are also presented (see Sect. 3.3).

| $i$ | $M_2(M_\odot)$ | $R_2(R_\odot)$ | $T_2$ (K) | $L_2/L_{2_{\rm mf}}$ | $d$ (kpc) |
|---|---|---|---|---|---|
| 31° | 7.89 | 9.29 | $1.7 \times 10^4$ | $\sim 0.02$ | $\geq 50$ |
| 35° | 6.20 | 8.58 | $1.5 \times 10^4$ | $\sim 0.11$ | $\geq 20$ |
| 40° | 4.87 | 7.91 | $1.2 \times 10^4$ | $\sim 0.55$ | $\geq 10$ |
| 44° | 4.17 | 7.51 | $9.5 \times 10^3$ | $\sim 1.0$ | $\geq 7$ |
| 50° | 3.45 | 7.10 | $8.6 \times 10^3$ | $\sim 2.2$ | $\geq 5$ |

$\lambda\lambda 8498, 8542, 8662$ triplet as an indicator of the detection limit of the secondary star, but the (possible) features were contaminated by emission lines of the Paschen series. Si III $\lambda 4525$ and Mg II $\lambda 4481$ were finally selected for an early B III secondary star ($i < 31°$) and a star between late B III and early F III ($35° < i < 50°$), respectively. The threshold of the detection limit of absorption features was determined as an equivalent width of $\sim 0.1$ Å corresponding to the noise to signal ratio at each wavelength range.

In case of $i < 31°$, from the invisibility of Si III $\lambda 4525$ with an equivalent width of $\sim 0.3$ Å for an early B III star in the spectrum, the flux ratio was derived as $f_2(\mathrm{B})/f(\mathrm{B}) \leq 2/3$, where $f_2(\mathrm{B})$ and $f(\mathrm{B})$ are the flux of the secondary star and the total flux of the system in the B-band, respectively. Then the bolometric luminosity ratio was estimated as $L_2/L \leq 1/16$, where $L_2$ and $L$ are a bolometric luminosity of the secondary star and the total bolometric luminosity of the system, respectively. If a distance to the object is assumed to be conservatively set to $d = 7$ kpc with a bolometric luminosity of $L \sim 2 \times 10^{35}(d/1\ \mathrm{kpc})^2\ \mathrm{erg\ s^{-1}}$ (Ebisawa et al. 1996), $L_2$ should be less than about $160\ L_\odot$. While, a bolometric luminosity of the secondary star based on the $M_2$–$R_2$ relation, i.e. the mass function, ($L_{2_{\rm mf}}$) is expected as $L_{2_{\rm mf}} \sim 6 \times 10^3\ L_\odot$ at $i = 31°$, which is larger than the observational upper limit of $L_2$ expected from the flux ratio. The case of $i < 31°$ could be therefore rejected, or at least a distance greater than 50 kpc is required for plausibility of this case.

In cases of $35° < i < 40°$ corresponding to a B8 III–A2 III secondary star, the upper limit of $L_2$ which was estimated from the comparison with the template spectra, here using the invisibility of Mg II $\lambda 4481$ with an equivalent width of $\sim 0.4$ Å, is less than the $L_{2_{\rm mf}}$ expected from the $M_2$–$R_2$ relation for any inclination angle of these cases. The luminosity ratio becomes larger than unity at $i \sim 44°$ corresponding to an A3 III secondary star, where roughly $L_2/L \leq 1/10$ and $L_2 \leq 550\ L_\odot$ at $d = 7$ kpc. Here, $L_{2_{\rm mf}} \sim 540\ L_\odot$ is expected at $i = 44°$ from the $M_2$–$R_2$ relation, which is comparable to the upper limit of the $L_2$ guessed from the flux ratio. The cases of $i < 44°$ could be therefore considered to be rejectable. The constraints derived by the method are summarized in Table. 4.

Eclipses have not been detected in X-ray and optical wavelengths for the object, but this result is not conclussive because of the sparse data distribution and the relatively long orbital pe-

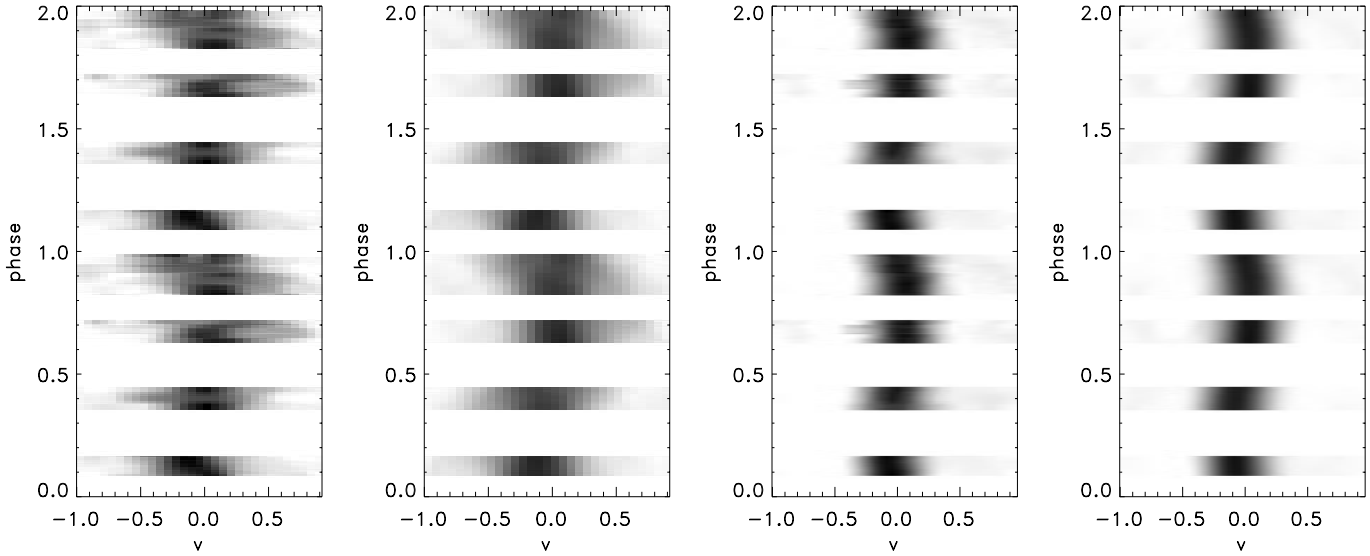


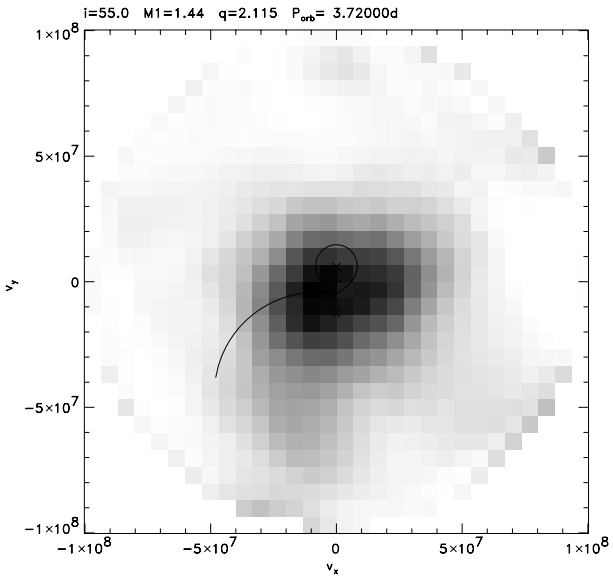


**Fig. 5.** Top: The trailed sequence of the observed (left) and reconstructed (right) spectra of the He II $\lambda 4686$ emission line. The horizontal axis represents a relative velocity ($10^8$ cm s$^{-1}$). Bottom: The Doppler map of He II $\lambda 4686$. The horizontal and vertical axes represent the velocity (cm s$^{-1}$). The stream and lobe drawn in the map were based on the binary parameters derived from the mass function and are only given as a reference.

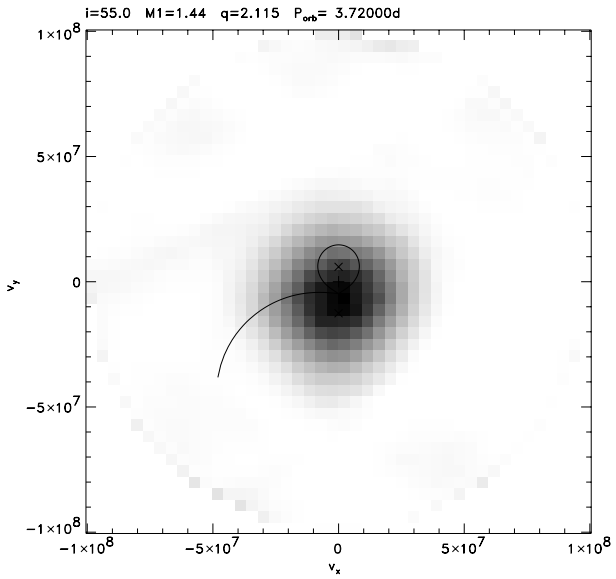


**Fig. 6.** Top: The trailed sequence of the H$\alpha$ emission line. Bottom: The Doppler map of H$\alpha$. The styles of the figures are same as those of Fig. 5.

riod. In the case of a non-eclipsing white dwarf, the inclination angle of the binary system should be less than $\sim 65°$, and a corresponding A3–F6 giant secondary star is finally suggested. A later secondary around G giant is also acceptable if the distance is $\sim 4$ kpc, as suggested by Hartmann et al. (1999).

### *3.4. Doppler imaging*

In order to obtain positional information about origin of the emission lines in the binary system, Doppler maps were calculated for the He II $\lambda 4686$ and H$\alpha$ (see Marsh & Horne (1988) for a review of the Doppler tomography). The analyses were performed using a Doppler mapping and plotting program developed for accretion disks in binary systems by Spruit (1999).

The ephemeris based on the spectroscopic phase of the radial velocity curves was used to trail the phase for the spectral series. Fig. 5 and Fig. 6 show the Doppler maps of the He II $\lambda 4686$ and H$\alpha$, respectively, with the trailed spectral series. For drawing the positions and lobes, a temporary inclination angle of $55°$ and a 3.0 $M_\odot$ secondary star were assumed for a 1.44 $M_\odot$ white dwarf. These are shown for reference in the maps.

We found that the general features of the object resemble to those of RX J0019.8+2156 (Deufel et al. 1999). Although the phase resolution is sparse, the sinusoidal trailed spectra do not show signs of any S-wave component. Both Doppler maps immediately indicate that the main emitting sources concentrate

on around the center of the velocity space, being completely different to the maps of optically thin accretion disks. If the binary elements adopted here are at least roughly correct, the peak of the line emission distribution could evidence an irradiated secondary star.

The Doppler maps show that the dominant regions for both lines has $v_y \sim -100$ km s$^{-1}$ roughly corresponding to the middle of the two stars. For the $v_x$ axis, the H$\alpha$ emission is located around the center of gravity of the binary system. In contrast, the He II $\lambda 4686$ emission shows a peak at $v_x \sim -100$ km s$^{-1}$. This asymmetric structure of the helium line was also seen in RX J0019.8+2156, which may suggest a common character for origins of the helium emission lines among SSXSs.

The low-velocity concentration of the dominant emission source suggests that the radial velocity variation provides a lower limit of $M_2$. It has been pointed out that the expectations from radial velocity studies in SSXSs may be essentially difficult and such a difficulty was also suggested in this object (Motch 1996). Van den Heuvel et al. (1992) suggested that a radial velocity of He II $\lambda 4686$ may not reflect correctly the orbital motion of the emitting component in SSXSs. In the case of RX J0019.8+2156, Deufel et al. (1999) concluded that the modulations of the main emission lines did not reflect the motions of the accretion disk but the low velocity regions. We also argued that some doubt may be casted on the assumption that the radial velocity variation simply reflects the orbital motion in this object and it may be probable that the true $K_1$ value in the binary system is larger than that of the He II $\lambda 4686$. The possible upper limit of the inclination angle is little different within, at least, the error of $K_1$. Thus the possible range of the secondary star may be more restricted to the hotter side in such a case.

*Acknowledgements.* The authors would like to express their sincere gratitude to Tariq Shahbaz for providing the additional data set. This work is partly supported by the Hayakawa-Yukio Foundation of the Astronomical Society of Japan, and the Research Fellowships of the Japan Society for the Promotion of Science for Young Scientists (K.M.), and Fondecyt 1971064, DI UdeC 99.11.28-1 and the National Science Foundation through grant number GF-1002-98 from the Association of Universities for Research in Astronomy, Inc., under NSF Cooperative Agreement No. AST-8947990 (R.M.).

## References

Becker C.M., Remillard R.A., Rappaport S.A., McClintock J.E., 1998, ApJ 506, 880
Crampton D., Hutchings J.B., Cowley A.P., et al., 1996, ApJ 456, 320
Deufel B., Barwig H., Šimić D., Wolf S., Drory N., 1999, A&A 343, 455
Ebisawa K., Asai K., Mukai K., et al., 1996, In: Greiner J. (ed.) Supersoft X-Ray Sources. Lecture Notes in Physics 472, Springer-Verlag, p. 91
Hachisu I., Kato M., Nomoto K., Umeda H., 1999, ApJ 519, 314
Hartmann H.W., Heise J., Kahabka P., Motch C., Parmar A.N., 1999, A&A 346, 125
Hoshi R., 1998, PASJ 50, 501
Jacoby G.H., Hunter D.A., Christian C.A., 1984, ApJS 56, 257
Kahabka P., van den Heuvel E.P.J., 1997, ARA&A 35, 69
Katahira J., Hirata R., Ito M, et al., 1996, PASJ 48, 317
Li X.-D., van den Heuvel E.P.J., 1997, A&A 322, L9
Marsh T.R., Horne K., 1988, MNRAS 235, 269
Motch C., 1996, In: Greiner J. (ed.) Supersoft X-Ray Sources. Lecture Notes in Physics 472, Springer-Verlag, p. 83
Motch C., 1998, A&A 338, L13
Motch C., Hasinger G., Pietsch W., 1994, A&A 284, 827
Rappaport S., Di Stefano R., Smith J.D., 1994, ApJ 426, 692
Silva D.R., Cornell M.E., 1992, ApJS 81, 865
Spruit H.C., 1999, http://www.mpa-garching.mpg.de/∼henk/
Tomov T., Munari U., Kolev D., Tomasella L., Rejkuba M., 1998, A&A 333, L67
van den Heuvel E.P.J., Bhattacharya D., Nomoto K., Rappaport S.A., 1992, A&A 262, 97